

Boosting segmentation with weak supervision from image-to-image translation

Eugene Vorontsov^{*1,2}, Pavlo Molchanov³, Wonmin Byeon³, Shalini De Mello³, Varun Jampani³, Ming-Yu Liu³, Samuel Kadoury², and Jan Kautz³

¹École Polytechnique de Montréal, ²Mila, ³NVIDIA

Abstract

In many cases, especially with medical images, it is prohibitively challenging to produce a sufficiently large training sample of pixel-level annotations to train deep neural networks for semantic image segmentation. On the other hand, some information is often known about the contents of images. We leverage information on whether an image presents the segmentation target or whether it is absent from the image to improve segmentation performance by augmenting the amount of data usable for model training. Specifically, we propose a semi-supervised framework that employs image-to-image translation between weak labels (e.g., presence vs. absence of cancer), in addition to fully supervised segmentation on some examples. We conjecture that this translation objective is well aligned with the segmentation objective as both require the same disentangling of image variations. Building on prior image-to-image translation work, we re-use the encoder and decoders for translating in either direction between two domains, employing a strategy of selectively decoding domain-specific variations. For presence vs. absence domains, the encoder produces variations that are common to both and those unique to the presence domain. Furthermore, we successfully re-use one of the decoders used in translation for segmentation. We validate the proposed method on synthetic tasks of varying difficulty as well as on the real task of brain tumor segmentation in magnetic resonance images, where we show significant improvements over standard semi-supervised training with autoencoding.

1. Introduction

Semantic object segmentation from natural images is known to perform well with deep neural networks but these require a large quantity of pixel-level annotations. Obtaining a sufficient quantity of annotations is difficult and some-

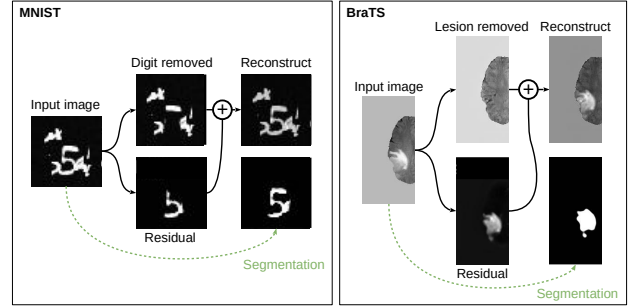


Figure 1: *Left*: Images presenting digits transformed to images with only the background clutter, a residual image that isolates the digit, and a segmentation of the digit. *Right*: Images presenting cancer lesions in the brain are transformed to healthy images, a residual image that isolates the lesion, and a segmentation of the lesion.

times impractical; on the other hand, unlabeled or weakly categorized data is easier to obtain. This motivates the need for weakly or semi-supervised models, to leverage unlabeled or weakly labeled data.

Many works have explored the use of generative adversarial networks (GANs) to improve semantic segmentation of medical images. However, while these methods make better use of the training data by either improving the training objective [23, 9, 42, 30, 39, 47, 43, 35, 25] or performing data augmentation within the training set [14, 31, 20], they do not augment the training set to better cover the variations in the data population. On the other hand, some works have explored unsupervised anomaly localization using autoencoding [5] or GANs [37, 7] to learn a generative model of healthy cases. Another GAN based approach is to train an error model that could be used for updates on unlabeled data [45]. These approaches are approximate and do not make full use of available weak labels (healthy and sick domain labels). Making better use of available data, some recent approaches relied on image-to-image translation between sick

^{*}Work done while author was interning at NVIDIA.

and healthy cases [4, 2] but these were unsupervised and either approximate or not validated against baselines or on multiple tasks.

We focus on the common scenario in medical imaging, where a large number of images lack segmentation labels but are known to be either healthy or sick cases. This knowledge can be considered as weak proxy labels that identify whether there is something to be segmented in an image. For example, when segmenting cancerous lesions, images marked ‘healthy’ do not contain cancer while images marked ‘sick’ do. We argue that the objective of translating from sick to healthy images is a good unsupervised surrogate for segmentation. Consequently, we develop a semi-supervised segmentation method with image-to-image translation, trained on unpaired images from sick and healthy domains.

Considering the sick domain as a superset of the variations in the healthy domain, we encode images into two latent codes: variations that are *common* to both and variations that are *unique* to the sick domain. This allows us to split decoding into two parts: (1) a ‘healthy’ image decoder that interprets the *common* latent code and (2) a residual decoder that additionally considers the *unique* code in order to compute a residual change to the ‘healthy’ output image, making it ‘sick’.

Because the output of the residual decoder is highly correlated with the segmentation output we can re-use the decoder for segmentation. In doing so, we maximize the proportion of model parameters that receive updates even when there are no pixel-level annotations available to guide image segmentation during training. Examples of these mappings, including both decoders and the segmentation output, are shown in Figure 1. Furthermore, whereas image-to-image translation models do not use long skip connections from the encoder to the decoder, we propose a long skip connection variant in our method. Long skip connections are common with supervised encoder-decoder models [10], where they help preserve spatial detail in the decoder even when the encoding is very deep. Overall, we summarize our contributions as follows:

- We propose a semi-supervised segmentation method leveraging image-to-image translation.
- We propose the use of (new) long skip connections for image-to-image translation, from encoder to decoder.
- We propose a dual-function decoder (translation, segmentation), thus maximizing the number of parameters updated in the absence of pixel-level annotations.
- We validate our method on challenging synthetic data and real brain tumor MR images, significantly improving over well-tuned baselines.

2. Related works

Image-to-image translation. Image to image translation was most prominently done with the CycleGAN [46] which does bidirectional translation between two domains. UNIT [26] proposed a similar approach but with a common latent space, shared by both domains, from which latent codes could be sampled. Augmented CycleGAN [1] and Multimodal UNIT [19] respectively extended both methods from one-to-one mappings to many-to-many.

Disentangling domain-specific variations. Both [19] and [24] present methods that learn shared and domain-specific latent codes. These differ from the proposed method in that they do not segment and do not assume (and benefit from) an *absence* domain as a subset of a *presence* domain. In addition, the domain-specific “style” codes are encoded with a shallow network which may bias the model to indeed learn domain-specific styles; whereas, the proposed method uses deep encodings for all codes. Explicit disentangling of variations between these codes has recently been proposed in [13] by way of a gradient reversal layer [12].

Data Augmentation. GANs are used to augment liver lesion examples for classification in [11]. [22] synthesize data to cover uncommon cases such as peripheral nodules touching the lung boundary. [14] and [31] introduce a segmentation mask generator to augment small training datasets.

Anomaly localization. Generative models have been used to fit the distribution of healthy images in order to find anomalies. To localize lesions in brain MR images that are known to be either healthy or sick, [5] fit the healthy data distribution with an autoencoder. Given an image presenting a lesion, the lesion is localized via the residual of its reconstructed image which is likely to appear healthy. Similarly, [37] and [7] employ GAN to locate anomalies in retinal images and brain MR images, respectively. While these models require that weak ‘sick’ or ‘healthy’ labels are known, they are trained only on the latter. Furthermore, they allow only rough unsupervised localization.

Image-to-image translation for segmentation. By translating from sick to healthy images, [4] trains a network to localize Alzheimer’s derived brain morphological changes using the output residual. [2] further proposes a multimodal variant of CycleGAN [46] to translate in both directions, applied to brain MR images with cancer. Sick images that are translated to healthy images are translated back to the original sick image via a residual inpainting of the lesions. Lesions are localized and segmented by predicting a minimal region to which to apply inpainting. Segmentation is unsupervised, with a prior that minimizes the inpainting region. This method has not been compared to other unsupervised methods, has been tested on a single dataset, and has not been extended to a weakly- or semi-

supervised setting. Our work differs in that we develop a semi-supervised architecture that uses fewer parameters by reusing mappings, we skip information from the encoder to decoders, we propose a decoder that is trained with both translation and segmentation objectives, and we validate the method on multiple tasks.

Adversarial semi-supervised segmentation. A semi-supervised segmentation method for medical images was proposed by [45], where a discriminator learns a segmentation error signal on the annotated dataset which can be applied on unannotated data. This method may be limited in how well it could scale with the proportion of unannotated data since the discriminator’s behaviour may not generalize well beyond the annotated dataset on which it is trained. Because this method can be applied to the output of any segmentation model, we consider it complementary to our proposed method.

3. Methods

Segmentation labels are typically available for an insufficiently representative sample of data. We propose a semi-supervised method that extends supervised segmentation to weakly labeled data using a domain translation objective. In addition to a segmentation objective, the method attempts to translate between the distribution of images presenting the segmentation target (P) and the distribution of images where this target is absent (A).

3.1. Translation, segmentation, and autoencoding

Translating between images where the segmentation target object is present or absent requires a model to localize the target. It follows then that in order to add, remove, or modify the target in an image, the variations caused by it should be disentangled from everything else (Figure 2, left). We conjecture that segmentation relies on the same disentangling and that this is the most difficult part of both objectives. Thus, we identify domain translation as an unsupervised surrogate loss for segmentation. We propose an encoder-decoder model that extends segmentation with image-to-image translation. In addition, we leverage the similarity between these two objectives to employ a decoder that is shared by both.

Although domain translation aligns well with segmentation, the canonical objective for unsupervised feature learning is autoencoding of the model input. A deep autoencoder may disentangle causal features of an image; that is, encoding the image may yield information about the features that produce it (Figure 2, right). When labels could be considered to cause the image, one would expect autoencoding to learn features that are useful for classification or segmentation [38]. Indeed, [32] recently won the Brain Tumor Segmentation challenge (2018) by augmenting a fully

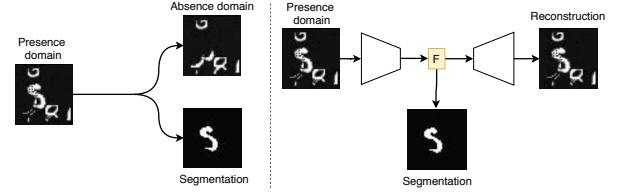


Figure 2: *Left:* Translating images from a domain presenting the segmentation target object (Presence) to one in which it is absent (Absent) involves disentangling the object’s variations from the rest. The former is useful for segmentation, the latter for producing an image without the object. *Right:* Autoencoding may produce disentangled features (F) that are useful but not optimal for segmentation.

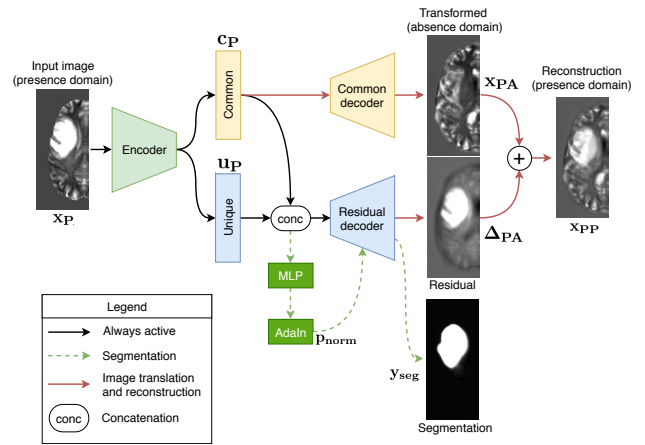


Figure 3: Framework overview of simultaneous segmentation, image translation and reconstruction. Images are transformed from the *presence* domain into the *absence* domain. Transformations are evaluated by a discriminator (not shown). The encoder and each decoder share skip connections for higher quality image generation.

convolutional segmentation network with an autoencoding objective. This objective is easy to set up and train for. Unlike with domain translation, no knowledge about the images’ domain is required. On the other hand, information about presence (P) or absence (A) of the segmentation target in the image may guide a domain translation objective to more specifically isolate the variations that are important for segmentation [13].

3.2. Our method

The proposed model builds on an encoder-decoder fully convolutional network (FCN) segmentation setup by introducing translation between a domain of images presenting the segmentation target (P) and a domain where it is absent (A), as in Figure 3. The encoder separates variations into those that are *common* to both A and P and those that are

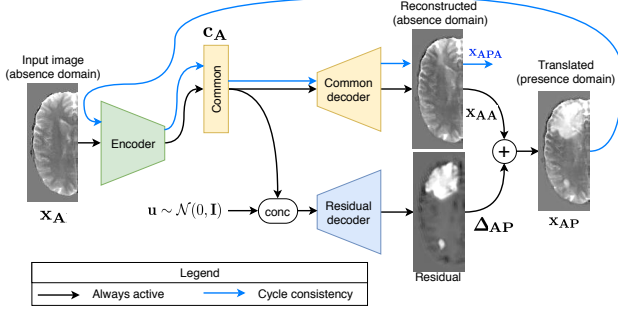


Figure 4: Image-to-image translation from the *absence* domain to the *presence* domain. The common code extracted by the encoder is used to reconstruct the input image. The unique code is sampled from a Normal distribution and concatenated to the common code to produce a residual image which, when added to the reconstructed image, yields a new image in the *presence* domain. We cycle the image back through the encoder and the common decoder to ensure that the reconstructed image remains unchanged.

unique to P; essentially, P is a superset of the variations in A. For example, in the case of medical images of cancer, both A and P contain the same organs but P additionally contains cancerous lesions.

Latent code decomposition. Starting with images \mathbf{x} in domains A or P, the encoder (f) yields *common* (\mathbf{c}) and *unique* (\mathbf{u}) codes:

$$\begin{aligned} [\mathbf{c}_A, \mathbf{u}_A] &= f(\mathbf{x}_A), \\ [\mathbf{c}_P, \mathbf{u}_P] &= f(\mathbf{x}_P). \end{aligned} \quad (1)$$

This decomposition of the latent codes is reminiscent of the *style* and *content* decomposition in [19] or the domain-specific codes in [24].

Presence to absence translation. Translation is achieved by selectively decoding from the latent codes \mathbf{c} and \mathbf{u} . A *common* decoder (g_{com}) uses only common variations, \mathbf{c} , to generate images in A:

$$\begin{aligned} \mathbf{x}_{AA} &= g_{com}(\mathbf{c}_A), \\ \mathbf{x}_{PA} &= g_{com}(\mathbf{c}_P), \end{aligned} \quad (2)$$

where \mathbf{x}_{AA} is essentially an autoencoding of \mathbf{x}_A , whereas \mathbf{x}_{PA} is a translation of \mathbf{x}_P to the A domain where the segmentation target is removed. With this translation, the target variations can be recovered separately, by computing a residual change Δ_{PA} to \mathbf{x}_{PA} that reconstructs \mathbf{x}_P as \mathbf{x}_{PP} . This is done with a second *residual* decoder (g_{res}) which uses both common variations and those unique to P (see Figure 3):

$$\begin{aligned} \mathbf{x}_{PP} &= \mathbf{x}_{PA} + \Delta_{PA}, \\ \Delta_{PA} &= g_{res}(\mathbf{c}_P, \mathbf{u}_P). \end{aligned} \quad (3)$$

The residual decoder requires all latent codes, $\{\mathbf{c}_P, \mathbf{u}_P\}$, as its input because the manifestation of unique variations in the image space is dependent on the common variations. For example, the way cancer manifests in a brain scan depends on the location and structure of the brain in the scan. Note also that because the common decoder only uses the common latent code, the encoder must learn to disentangle common and unique variations.

Segmentation. The \mathbf{c}_P and \mathbf{u}_P codes or the Δ_{PA} residual contain sufficient information for segmentation. Indeed we reuse the residual decoder, used with \mathbf{x}_P , for segmentation. We parameterize a segmentation decoder g_{seg} in terms of the residual decoder g_{res} , with segmentation specific per-layer instance normalization [40] parameters \mathbf{p}_{norm} :

$$\begin{aligned} \mathbf{y}_{seg} &= g_{seg}(\mathbf{c}_P, \mathbf{u}_P), \\ &= (\hat{g}_{res} \circ s)(\mathbf{c}_P, \mathbf{u}_P), \end{aligned} \quad (4)$$

where s is a pixelwise classification layer and \hat{g}_{res} is a subset of the g_{res} network that contains all but the last layer, using normalization parameters produced from the latent code by a multi-layer perceptron (MLP):

$$\mathbf{p}_{norm} = MLP(\mathbf{c}_P, \mathbf{u}_P). \quad (5)$$

Absence to presence translation. Finally, we conclude the set of autoencoding and translation equations with \mathbf{x}_{AP} and \mathbf{x}_{APA} , where images in A are translated to images in P (Figure 4). We note that although these translations are not useful for segmentation, they are useful during training since they effectively augment the training updates that our encoders and decoders can receive. Since P contains additional variations to those found in A, we must either add these variations from an image in A or sample them from a prior distribution:

$$\begin{aligned} \mathbf{x}_{AP} &= g_{com}(\mathbf{c}_A) + g_{res}(\mathbf{u} \sim \mathcal{N}(0, \mathbf{I})), \\ \mathbf{x}_{APA} &= g_{com}(\mathbf{c}_AP), \\ [\mathbf{c}_{AP}, \mathbf{u}_{AP}] &= f(\mathbf{x}_{AP}). \end{aligned} \quad (6)$$

Here, \mathbf{x}_{AP} requires a sample \mathbf{u} from a zero-mean, unit variance prior over the unique variations, $\mathcal{N}(0, \mathbf{I})$. Note that unlike in a variational autoencoder, the encoder f does not parameterize a conditional distribution over the unique variations but rather encodes a sample directly. We ensure that the distribution of encoded samples matches the prior by making \mathbf{u}_{AP} match \mathbf{u} , as detailed further in the description of our training objective. The translation of \mathbf{x}_{AP} to \mathbf{x}_{APA} completes a cycle as in [46]. When \mathbf{x}_{APA} must match \mathbf{x}_A , this ensures that the translations retain information about their source images, ensuring that the encoder and decoders do not learn trivial functions. As shall be seen below, this is already achieved by other objectives, making the cycle optional.

Total loss. The training objective consists of a segmentation loss L_{seg} combined with four translation losses, each weighted by some scalar λ :

$$L_{total} = L_{seg} + \lambda_{rec} L_{rec} + \lambda_{lat} L_{lat} + \lambda_{cyc} L_{cyc} + \lambda_{adv} L_{adv}. \quad (7)$$

Segmentation loss. We use Dice loss for segmentation, as in [10, 28], which measures the overlap between the predicted segmentation \mathbf{y} and reference segmentation $\hat{\mathbf{y}}$:

$$L_{seg} = \text{Dice}(\mathbf{y}, \hat{\mathbf{y}}). \quad (8)$$

Reconstruction losses. To ensure that the encoder and decoders can cover the distribution of images, we reconstruct input images:

$$L_{rec} = L_{rec}(\mathbf{x}_P, \mathbf{x}_{PP}) + L_{rec}(\mathbf{x}_A, \mathbf{x}_{AA}). \quad (9)$$

Similarly, we reconstruct the latent codes so as to ensure that their distributions match across domains A and P, or in the case of unique codes, match the prior:

$$\begin{aligned} L_{lat} = & L_{lat}(\mathbf{c}_P, \mathbf{c}_{PA}) + L_{lat}(\mathbf{c}_A, \mathbf{c}_{AP}) \\ & + L_{lat}(\mathbf{c}_A, \mathbf{c}_{AA}) + L_{lat}(\mathbf{c}_P, \mathbf{c}_{PP}) \\ & + L_{lat}(\mathbf{u}_P, \mathbf{u}_{PP}) + L_{lat}(\mathbf{u}, \mathbf{u}_{AP}). \end{aligned} \quad (10)$$

We define a cycle consistency loss for the APA cycle:

$$L_{cyc} = L_{rec}(\mathbf{x}_A, \mathbf{x}_{APA}). \quad (11)$$

Note that there is no PAP cycle since in the proposed method this is equivalent to PP reconstruction, as can be seen in Figure 3. Because both images and the their latent codes are reconstructed, the cycle consistency loss is optional.

We use the L_1 distance for all reconstruction losses.

Adversarial loss. Finally, we use the hinge loss for the adversarial objective, together with spectral norm on the encoder and decoders as in [44]:

$$\begin{aligned} L_{adv} = & \sum_{d \in \{A, P\}} \min_G \max_D \left[\right. \\ & - \mathbb{E}_{\mathbf{x}_d \sim p_d} [\min(0, D_d(\mathbf{x}_d) - 1)] \\ & - \mathbb{E}_{\hat{\mathbf{x}}_d \sim \hat{p}_d} [\min(0, -D_d(G_d(\hat{\mathbf{x}}_d)) - 1)] \\ & \left. - \mathbb{E}_{\hat{\mathbf{x}}_d \sim \hat{p}_d} D_d(G_d(\hat{\mathbf{x}}_d)) \right], \end{aligned} \quad (12)$$

where, for each domain $d \in \{A, P\}$, G_d is the generator network for some generated image $\hat{\mathbf{x}}_d \sim \hat{p}_d$ and D_d is a discriminator network which discriminates between real data $\mathbf{x}_d \sim p_d$ and generated data $\hat{\mathbf{x}}_d$.

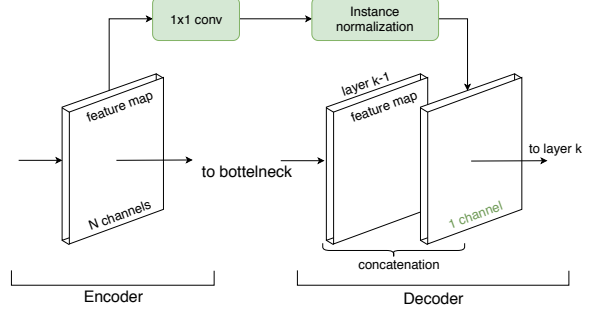


Figure 5: Compressed skip connection as a way to limit information bypass while preserving spatial detail.

3.3. Baseline methods

The proposed method is compared against two baseline approaches: a fully supervised, fully convolutional network (FCN) and another one augmented with a reconstruction objective for semi-supervised training. To ease comparison, all models (baselines and proposed) share the same encoder and decoder architectures. The fully supervised method uses an encoder with a single decoder (“Segmentation only” in Table 1). This is equivalent to the proposed method with only the segmentation loss, using only the residual decoder. The semi-supervised method (“AE baseline” in Table 1), adds an additional decoder that reconstructs the input.

3.4. Compressed long skip connections

In all models, including baselines, every decoder accepts long skip connections from the encoder, as in [10]. These connections skip features from each layer in the encoder to the corresponding layer in the decoder, except for the first and the last layers. Because long skip connections make autoencoding trivial, they are not used with the reconstruction decoder in the semi-supervised baseline method, however skip connections are used between the encoder and segmentation decoder.

Typically, feature maps from the encoder are either directly summed with [10] or concatenated to [36] those in the decoder. We proposed a modified variant of long skip connections where any stack of feature maps is first compressed (via 1×1 convolution) to a single map before concatenation (see Figure 5). We note that concatenating all feature maps is costly computationally and appears to increase training time for image translation whereas summing feature maps makes the image translation task very difficult to learn. To further stabilize training, all features skipped from the encoder are normalized with instance normalization. We find that these long skip connections help train the model faster and help produce higher quality image outputs even with a deep encoder.

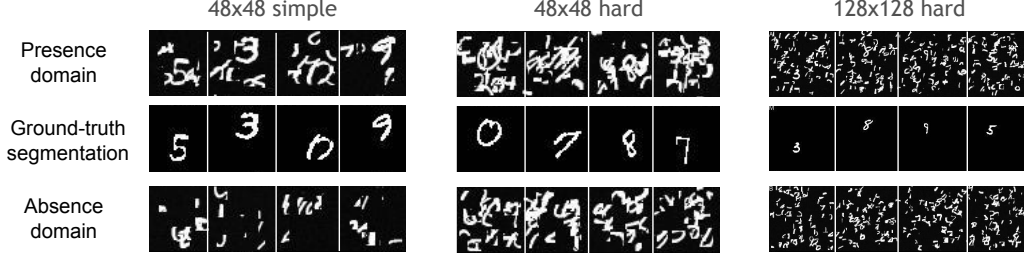


Figure 6: Examples of images from the synthetic MNIST datasets. Samples from the *presence* domain and corresponding ground truth segmentations are in the first and second rows; unrelated samples from the *absence* domain are in the third row.

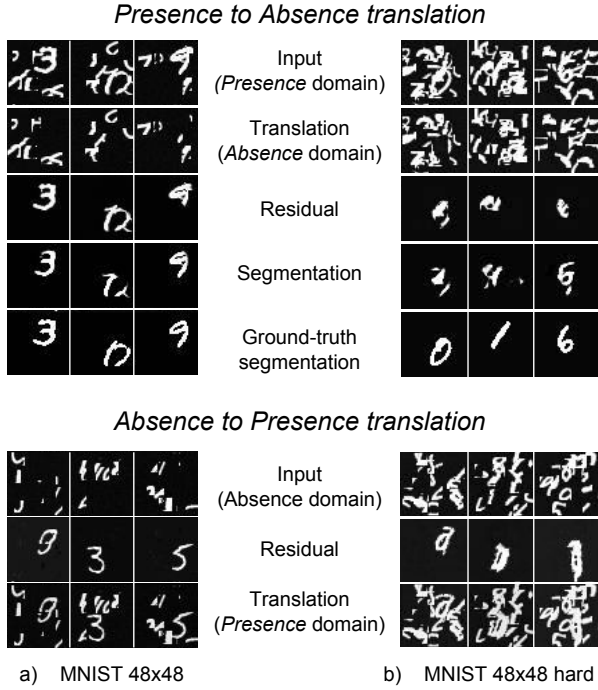


Figure 7: Example of image translation and segmentation for cluttered MNIST.

4. Experiments

In this section, we evaluate our proposed semi-supervised segmentation method on both synthetic and real data. We confirm that this method outperforms the fully supervised and semi-supervised segmentation baselines. We present examples of image translation results to illustrate the correlation between segmentation and image translation tasks. We begin with a synthetic MNIST-based task that simulates the common situation, where some images are known to present the segmentation target (P), while in others it is known to be absent (A). With this data, we experiment with increasing the difficulty of the segmentation task.

Then, we proceed to evaluate the proposed method on brain tumour segmentation on real MRI data (BraTS).

4.1. Cluttered MNIST

We construct a synthetic task for digit segmentation using MNIST digits, similar to the cluttered MNIST dataset in [21]. Each image in P contains a complete randomly positioned digit placed on a background of clutter. The clutter is produced from randomly cropped digits within the same data fold (training, validation, or test set). In all experiments, we used crops of 10x10 pixels. We dither regions where MNIST digits or clutter components overlap, so as to prevent models from identifying these boundaries.

We tested the proposed model and the baseline methods on three variants of the cluttered MNIST task, at two resolutions: 48×48 *simple*, with 8 pieces of clutter; 48×48 *hard*, with 24 pieces of clutter; and 128×128 , with 80 pieces of clutter. Samples from these generated datasets are shown in Figure 6; all datasets were generated prior to training. In all experiments, we provided reference segmentations for 1% of the training examples. In addition, to mimic the issue of small training datasets where the training set fails to cover all modes of variation of the data population, we trained on reference segmentations only for the digit 9.

As shown in Table 1, the proposed model significantly outperforms both the semi-supervised and the fully supervised baselines. The improvement is greater for the harder variants of the task: 48×48 *hard* and 128×128 . We suspect that the greater improvement on the 48×48 *hard* task may be due to the greater difficulty in separating digits from clutter as compared to 48×48 *simple*, in which case the translation objective that seeks to specifically disentangle digit variations from clutter variations should be particularly helpful.

Examples of image translation and segmentation are shown in Fig. 7. We first discuss *presence* to *absence* translation. For the MNIST 48×48 *simple* case, almost the entire digit is removed from the image during translation and the residual is similar to the segmentation result which supports our conjecture that translation is a good surrogate task

		MNIST		BraTS
	48×48 simple	48×48 hard	128×128	240×120
Only segmentation	0.61 (0.01)	0.36 (0.01)	0.15 (0.01)	0.69 (0.04)
AE baseline	0.75 (0.01)	0.49 (0.02)	0.57 (0.02)	0.73 (0.02)
Proposed	0.79 (0.01)	0.57 (0.00)	0.65 (0.01)	0.79 (0.02)

Table 1: Segmentation Dice scores for synthetic MNIST and real BraTS segmentation tasks: mean (standard deviation).

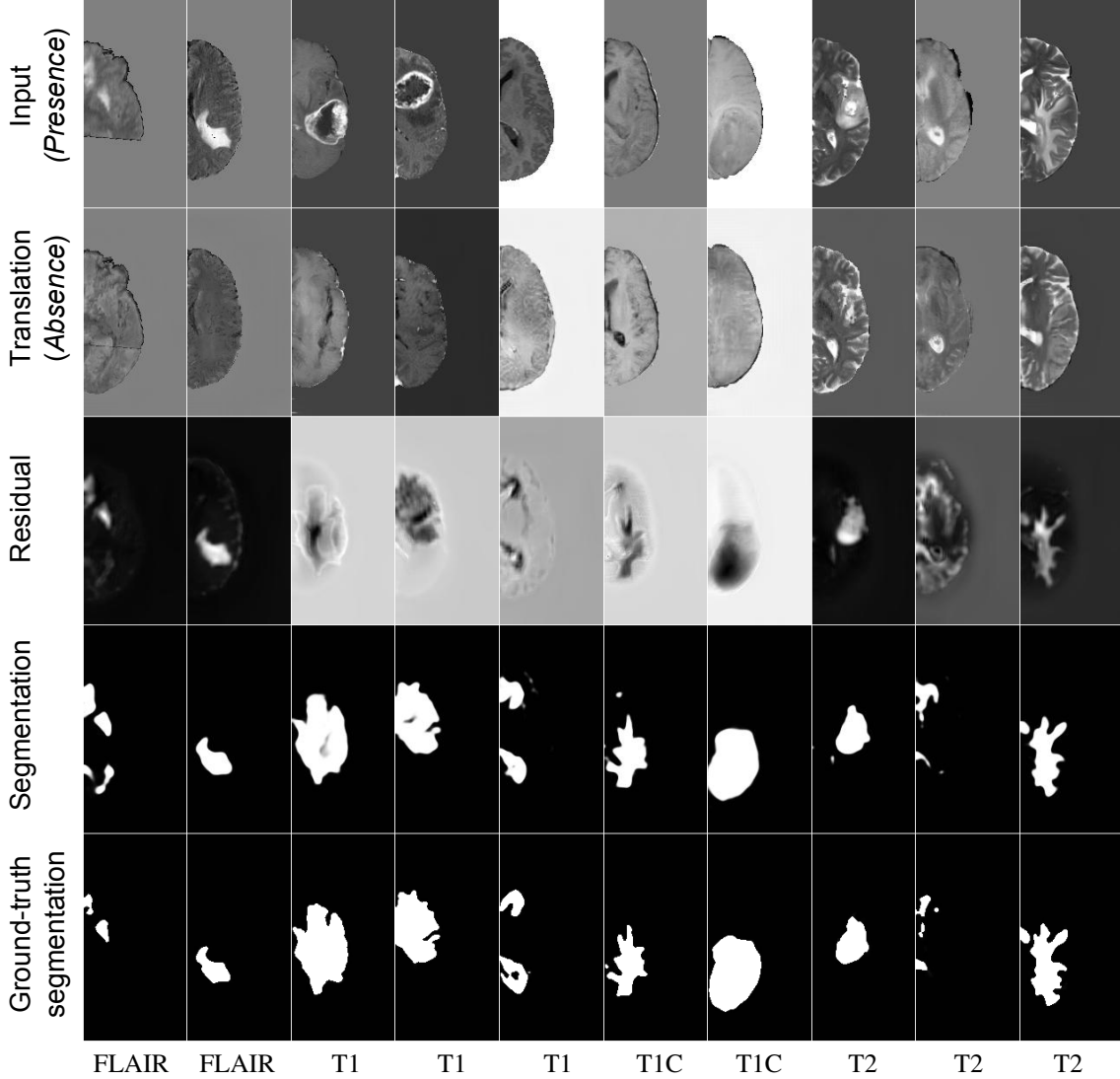


Figure 8: Example of image segmentation and translation from *Presence* to *Absence* domains for BraTS. Different MRI sequences (image channels) are arranged in columns.

for the segmentation task. The MNIST 48×48 hard dataset has very challenging images, in which localizing the true digit is very difficult even for people. The model learned to partially remove the digit in order to fulfill the GAN objective. Therefore, the residual does not contain the entire digit, however it attends to the correct location in the image

which may guide segmentation. We note that a digit does not need to be completely removed in order for the image to appear to contain only clutter because any remaining digit parts could appear as clutter. During *absence* to *presence* translation, the model learns the distribution of correct digits and is able to insert them into the image, as shown for

MNIST 48×48 *simple*. With more clutter (MNIST 48×48 *hard*) it becomes challenging; generated residuals have less variety and many look like variations of the digit 0.

These experiments demonstrate that semi-supervised segmentation benefits from image-to-image translation. We observed significant improvements over supervised and semi-supervised segmentation baselines.

4.2. BraTS

Moving beyond synthetic data, we evaluated the proposed method on brain tumour segmentation challenge 2017 data (BraTS). Because this dataset contains only magnetic resonance imaging (MRI) volumes presenting cancer, we artificially split the data along 2D axial slices into P and A domains as a proof of concept. Because lesions tend to be closer to the center of the brain than the top or bottom, slices from the center of the brain, containing more brain matter, tend to be over-represented in P as compared to A. We require that the P and A domains differ only in that P contains the segmentation target; therefore, in order to better balance the slice distributions between the two domains, we additionally split the brains into hemispheres and select only those half-slices that contain at least 25% brain pixels. In P, we also limit the minimal number of lesion pixels to 1% of brain pixels. We pre-process every volume by mean-centering the brain pixels (ignoring background) and dividing them by their standard deviation. Finally, we use half-slices extracted from the processed volumes as model inputs. Each input has four channels, corresponding to four registered MRI sequences: T1, T2, T1C, and FLAIR.

We trained the proposed model and baselines with reference labels available for 1% of the training data. As shown in Table 1, the proposed model achieves a 0.79 Dice score, significantly outperforming both the segmentation baseline, 0.69, and the semi-supervised autoencoding baseline, 0.79. Image translation and segmentation examples are shown in Figure 8. As evident in the figure, lesions were well removed by image-to-image translation. Unlike with the cluttered MNIST data, some of the sequences (T1, T1c) result in fairly complicated residuals that are nonetheless correctly reinterpreted as segmentations via the residual decoder.

The first column in Figure 8 reveals an artifact of distribution imbalance where a rare truncated input slice is transformed into a common non-truncated slice. Artifacts of this sort are particularly common when there is an imbalance in the distribution of slice sizes between P and A (which we try to avoid). Ideally, entire brain volumes would be used as inputs instead of slices.

5. Extensions and applications

Although we present work on two domains, P and A, we note that the proposed method can be easily extended to any greater number of domains. For example, if different types

of pathology are known to be present in a medical image dataset, a domain-specific code (with a corresponding residual decoder) could be encoded for each pathology in addition to a neutral code with any pathology absent. Most interestingly, our image-to-image translation approach would allow any number of pathologies to be present in an image at a time, unlike for example the StarGAN multi-domain image-to-image translation architecture [8].

Finally, we note that there are many different data outside of medical imaging that can be split into P and A domains. For example, any material fault analysis, such as rust detection, microchip defects, or the decay of building facades can be expressed that way. Another interesting application may be the surveying of flood damage by learning the difference between pre-flood and post-flood urban aerial images. Extending the proposed method to more than two domains, one could explore such multi-domain problems as shadow segmentation where different times of day constitute different domains (with noon in A).

6. Conclusion

We propose a semi-supervised segmentation method that makes use of image-to-image translation in order to leverage unsegmented training data with cases presenting the object (P) of interest and cases in which it is absent (A). We argue that this objective is a good unsupervised surrogate for segmentation because it should similarly rely on disentangling of object variations from other variations. Indeed, we validate our method on both synthetic cluttered MNIST segmentation tasks and brain tumour segmentation in MR images, where we achieve significant improvement over supervised segmentation and a semi-supervised baseline.

References

- [1] A. Almahairi, S. Rajeswar, A. Sordoni, P. Bachman, and A. Courville. Augmented cyclegan: Learning many-to-many mappings from unpaired data. *arXiv preprint arXiv:1802.10151*, 2018. 2
- [2] S. Andermatt, A. Horváth, S. Pezold, and P. Cattin. Pathology segmentation using distributional differences to images of healthy origin. *arXiv preprint arXiv:1805.10344*, 2018. 2
- [3] J. L. Ba, J. R. Kiros, and G. E. Hinton. Layer normalization. *arXiv preprint arXiv:1607.06450*, 2016. 11
- [4] C. F. Baumgartner, L. M. Koch, K. C. Tezcan, J. X. Ang, and E. Konukoglu. Visual feature attribution using wasserstein gans. *arXiv preprint arXiv:1711.08998*, 2017. 2
- [5] C. Baur, B. Wiestler, S. Albarqouni, and N. Navab. Deep autoencoding models for unsupervised anomaly segmentation in brain mr images. *arXiv preprint arXiv:1804.04488*, 2018. 1, 2
- [6] A. Brock, J. Donahue, and K. Simonyan. Large scale gan training for high fidelity natural image synthesis. *arXiv preprint arXiv:1809.11096*, 2018. 11

- [7] X. Chen and E. Konukoglu. Unsupervised detection of lesions in brain mri using constrained adversarial auto-encoders. *arXiv preprint arXiv:1806.04972*, 2018. 1, 2
- [8] Y. Choi, M. Choi, M. Kim, J.-W. Ha, S. Kim, and J. Choo. Stargan: Unified generative adversarial networks for multi-domain image-to-image translation. In *Proceedings of the IEEE Conference on Computer Vision and Pattern Recognition*, pages 8789–8797, 2018. 8
- [9] W. Dai, J. Doyle, X. Liang, H. Zhang, N. Dong, Y. Li, and E. P. Xing. Scan: Structure correcting adversarial network for chest x-rays organ segmentation. *arXiv preprint arXiv:1703.08770*, 2017. 1
- [10] M. Drozdal, E. Vorontsov, G. Chartrand, S. Kadoury, and C. Pal. The importance of skip connections in biomedical image segmentation. In *Deep Learning and Data Labeling for Medical Applications*, pages 179–187. Springer, 2016. 2, 5
- [11] M. Frid-Adar, I. Diamant, E. Klang, M. Amitai, J. Goldberger, and H. Greenspan. Gan-based synthetic medical image augmentation for increased cnn performance in liver lesion classification. *Neurocomputing*, 321:321–331, 2018. 2
- [12] Y. Ganin and V. Lempitsky. Unsupervised domain adaptation by backpropagation. In *International Conference on Machine Learning*, pages 1180–1189, 2015. 2
- [13] A. Gonzalez-Garcia, J. van de Weijer, and Y. Bengio. Image-to-image translation for cross-domain disentanglement. *arXiv preprint arXiv:1805.09730*, 2018. 2, 3
- [14] J. T. Guibas, T. S. Virdi, and P. S. Li. Synthetic medical images from dual generative adversarial networks. *arXiv preprint arXiv:1709.01872*, 2017. 1, 2
- [15] K. He, X. Zhang, S. Ren, and J. Sun. Delving deep into rectifiers: Surpassing human-level performance on imagenet classification. In *Proceedings of the IEEE international conference on computer vision*, pages 1026–1034, 2015. 10
- [16] K. He, X. Zhang, S. Ren, and J. Sun. Identity mappings in deep residual networks. In *European conference on computer vision*, pages 630–645. Springer, 2016. 10
- [17] M. Heusel, H. Ramsauer, T. Unterthiner, B. Nessler, and S. Hochreiter. Gans trained by a two time-scale update rule converge to a local nash equilibrium. In *Advances in Neural Information Processing Systems*, pages 6626–6637, 2017. 11
- [18] X. Huang and S. Belongie. Arbitrary style transfer in real-time with adaptive instance normalization. In *Proceedings of the IEEE International Conference on Computer Vision*, pages 1501–1510, 2017. 11
- [19] X. Huang, M.-Y. Liu, S. Belongie, and J. Kautz. Multimodal unsupervised image-to-image translation. *arXiv preprint arXiv:1804.04732*, 2018. 2, 4
- [20] S. Izadi, Z. Mirikharaji, J. Kawahara, and G. Hamarneh. Generative adversarial networks to segment skin lesions. In *2018 IEEE 15th International Symposium on Biomedical Imaging (ISBI 2018)*, pages 881–884. IEEE, 2018. 1
- [21] M. Jaderberg, K. Simonyan, A. Zisserman, et al. Spatial transformer networks. In *Advances in neural information processing systems*, pages 2017–2025, 2015. 6
- [22] D. Jin, Z. Xu, Y. Tang, A. P. Harrison, and D. J. Mollura. Ct-realistic lung nodule simulation from 3d conditional generative adversarial networks for robust lung segmentation. In *International Conference on Medical Image Computing and Computer-Assisted Intervention*, pages 732–740. Springer, 2018. 2
- [23] S. Kohl, D. Bonekamp, H.-P. Schlemmer, K. Yaqubi, M. Hohenfellner, B. Hadaschik, J.-P. Radtke, and K. Maier-Hein. Adversarial networks for the detection of aggressive prostate cancer. *arXiv preprint arXiv:1702.08014*, 2017. 1
- [24] H.-Y. Lee, H.-Y. Tseng, J.-B. Huang, M. Singh, and M.-H. Yang. Diverse image-to-image translation via disentangled representations. In *Proceedings of the European Conference on Computer Vision (ECCV)*, pages 35–51, 2018. 2, 4
- [25] Z. Li, Y. Wang, and J. Yu. Brain tumor segmentation using an adversarial network. In *International MICCAI Brainlesion Workshop*, pages 123–132. Springer, 2017. 1
- [26] M.-Y. Liu, T. Breuel, and J. Kautz. Unsupervised image-to-image translation networks. In *Advances in Neural Information Processing Systems*, pages 700–708, 2017. 2, 11
- [27] A. L. Maas, A. Y. Hannun, and A. Y. Ng. Rectifier nonlinearities improve neural network acoustic models. In *Proc. icml*, volume 30, page 3, 2013. 11
- [28] F. Milletari, N. Navab, and S.-A. Ahmadi. V-net: Fully convolutional neural networks for volumetric medical image segmentation. In *2016 Fourth International Conference on 3D Vision (3DV)*, pages 565–571. IEEE, 2016. 5
- [29] T. Miyato, T. Kataoka, M. Koyama, and Y. Yoshida. Spectral normalization for generative adversarial networks. *arXiv preprint arXiv:1802.05957*, 2018. 11
- [30] P. Moeskops, M. Veta, M. W. Lafarge, K. A. Eppenhof, and J. P. Pluim. Adversarial training and dilated convolutions for brain mri segmentation. In *Deep learning in medical image analysis and multimodal learning for clinical decision support*, pages 56–64. Springer, 2017. 1
- [31] T. C. Mok and A. C. Chung. Learning data augmentation for brain tumor segmentation with coarse-to-fine generative adversarial networks. In *International MICCAI Brainlesion Workshop*, pages 70–80. Springer, 2018. 1, 2
- [32] A. Myronenko. 3d mri brain tumor segmentation using autoencoder regularization. *arXiv preprint arXiv:1810.11654*, 2018. 3
- [33] A. Paszke, S. Gross, S. Chintala, G. Chanan, E. Yang, Z. DeVito, Z. Lin, A. Desmaison, L. Antiga, and A. Lerer. Automatic differentiation in pytorch. In *NIPS-W*, 2017. 10
- [34] S. J. Reddi, S. Kale, and S. Kumar. On the convergence of adam and beyond. 2018. 11
- [35] M. Rezaei, H. Yang, and C. Meinel. Whole heart and great vessel segmentation with context-aware of generative adversarial networks. In *Bildverarbeitung für die Medizin 2018*, pages 353–358. Springer, 2018. 1
- [36] O. Ronneberger, P. Fischer, and T. Brox. U-net: Convolutional networks for biomedical image segmentation. In *International Conference on Medical image computing and computer-assisted intervention*, pages 234–241. Springer, 2015. 5
- [37] T. Schlegl, P. Seeböck, S. M. Waldstein, U. Schmidt-Erfurth, and G. Langs. Unsupervised anomaly detection with generative adversarial networks to guide marker discovery. In *International Conference on Information Processing in Medical Imaging*, pages 146–157. Springer, 2017. 1, 2

- [38] B. Schölkopf, D. Janzing, J. Peters, E. Sgouritsa, K. Zhang, and J. Mooij. On causal and anticausal learning. In *Proceedings of the 29th International Conference on Machine Learning*, pages 459–466. Omnipress, 2012. 3
- [39] J. Son, S. J. Park, and K.-H. Jung. Retinal vessel segmentation in fundoscopic images with generative adversarial networks. *arXiv preprint arXiv:1706.09318*, 2017. 1
- [40] D. Ulyanov, A. Vedaldi, and V. Lempitsky. Instance normalization: The missing ingredient for fast stylization. *arXiv preprint arXiv:1607.08022*, 2016. 4, 11
- [41] T.-C. Wang, M.-Y. Liu, J.-Y. Zhu, A. Tao, J. Kautz, and B. Catanzaro. High-resolution image synthesis and semantic manipulation with conditional gans. In *Proceedings of the IEEE Conference on Computer Vision and Pattern Recognition*, pages 8798–8807, 2018. 11
- [42] Y. Xue, T. Xu, H. Zhang, L. R. Long, and X. Huang. Segan: Adversarial network with multi-scale l1 loss for medical image segmentation. *Neuroinformatics*, 16(3-4):383–392, 2018. 1
- [43] D. Yang, D. Xu, S. K. Zhou, B. Georgescu, M. Chen, S. Grbic, D. Metaxas, and D. Comaniciu. Automatic liver segmentation using an adversarial image-to-image network. In *International Conference on Medical Image Computing and Computer-Assisted Intervention*, pages 507–515. Springer, 2017. 1
- [44] H. Zhang, I. Goodfellow, D. Metaxas, and A. Odena. Self-attention generative adversarial networks. *arXiv preprint arXiv:1805.08318*, 2018. 5, 11
- [45] Y. Zhang, L. Yang, J. Chen, M. Fredericksen, D. P. Hughes, and D. Z. Chen. Deep adversarial networks for biomedical image segmentation utilizing unannotated images. In *International Conference on Medical Image Computing and Computer-Assisted Intervention*, pages 408–416. Springer, 2017. 1, 3
- [46] J.-Y. Zhu, T. Park, P. Isola, and A. A. Efros. Unpaired image-to-image translation using cycle-consistent adversarial networks. In *IEEE International Conference on Computer Vision*, 2017. 2, 4
- [47] W. Zhu, X. Xiang, T. D. Tran, and X. Xie. Adversarial deep structural networks for mammographic mass segmentation. *arXiv preprint arXiv:1612.05970*, 2016. 1

Appendix

A. Model and training details

This section details model architectures, parameter initializations, and optimization hyperparameters. Network layers are described in Tables 2-9. Here, *conv block* refers to a residual layer (as in the ResNet [16]) that chains together a normalization operation, an activation function, and a convolution, with a *short skip* connection from the input to the output as shown in in Figure 9. For all experiments we use PyTorch [33].

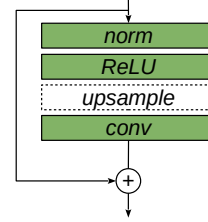


Figure 9: The *conv block* chains a normalization operation (norm), a rectified linear unit (ReLU), and a convolution (conv). When used in a decoder, $2\times$ upsampling is performed prior to convolution by simple repetition of pixel rows and columns. The input is summed to the output via a *short skip* connection.

General model structure The proposed model has one encoder and two decoders: *common* and *residual*. Additionally, it uses two discriminators, one for each direction of translation. The autoencoding baseline has one encoder and two decoders: segmentation and reconstruction. The segmentation baseline has one encoder and one segmentation decoder.

Reusing encoders and decoders. To compare the effect of different training objectives, we try to reduce the confounding effect of differing architectures between the proposed model and baseline models. For each task, we use the same encoder for all models; likewise, the *common* decoder in the proposed model and all decoders in the baseline models are the same. The *residual* decoder in the proposed model is similar, differing in that it lacks short skip connections and uses slightly larger convolution kernels. All encoders and decoders are initialized with the Kaiming Normal approach [15]. Convolutions are applied to inputs with reflection padding. All activation functions are rectified linear units (ReLU).

Skip connections. We use *long skip* connections from the encoder to every decoder except the reconstruction decoder of the autoencoding baseline. Long skip connections bridge representations of the same resolution (these have the same number of channels). Specifically, the representation in the encoder is compressed to a single channel with a 1×1 convolution and then concatenated to the corresponding decoder representation. The encoder and all decoders have *short skip* connections (as in the ResNet), except for the *residual* decoders of the proposed model.

Latent code split. All latent bottleneck representations of every model have 512 channels. In the proposed model, 128 of these channels are specified as the *residual* latent code and the rest as the *common* latent code.

Normalization. All encoders use instance normalization [40]. All decoders use layer normalization [3]. The *residual* decoder of the proposed model performs segmentation by adopting a segmentation-specific optimization approach that differs from the layer normalization used with translation.

Segmentation via residual decoder. In the proposed method, the *residual* decoder is used both in translation and in segmentation. For segmentation, all but the last layer are used and a classification layer is appended: 1×1 convolution with N channels, where N is the number of classes. In order to adapt the features learned via translation to the segmentation task, inference is modified by using a different normalization approach during segmentation than during translation. For the MNIST tasks, a four layer multi-layer perceptron with 256 units per layer is used to map the latent code (both *common* and *unique*) to parameters for adaptive instance normalization [18] in the *residual* decoder. For BraTS segmentation, the *residual* decoder uses separate layer normalization parameters for segmentation.

Discriminator. Two discriminators are used with the proposed method, one for each direction of translation. We use multi-scale discriminators as proposed in [41, 26]. The discriminator architectures shown in Table 8 and Table 9 describe the network that is applied at each of three scales. At some scales, discriminators output a map of values per image instead of a single value. First, all pixels in this map are averaged and second, the resulting discriminator values are averaged across all scales. All discriminators use leaky ReLU [27] with a slope of 0.2.

Optimization. For all experiments, we used the AMS-Grad optimizer [34] with $\beta_1 = 0.5$ and $\beta_2 = 0.999$. We used a learning rate of 0.0001 for all networks except discriminators which were trained with a learning rate of 0.001, following [17]. We used a batch size of 20 images. For MNIST experiments, we ran training for 300 epochs; for BraTS, 500 epochs. In the proposed method, we used the hinge loss for the adversarial objective, with spectral normalization [29] applied to all networks, as in [44, 6].

Weighted objectives. We found that the following objective weights yielded the best overall performance: $\lambda_{avd} = 3$, $\lambda_{rec} = 50$, $\lambda_{lat} = 1$, $\lambda_{cyc} = 50$, $\lambda_{seg} = 0.01$. (AE: $\lambda_{rec} = \lambda_{seg} = 1$).

Data augmentation We applied data augmentation on the fly during training for BraTS but not for MNIST tasks since a large amount of data is generated for the latter. Data augmentation involved random rotations up to 3 degrees, ran-

dom zooms up to 10% in or out, random intensity shifts up to 10%, random horizontal and/or vertical flips, and spline warping. Spline warping used a 3×3 grid of control points with each point placed according to a Normal distribution with variance $\sigma = 5$. In those cases where data augmentation created new pixels along image edges or corners, these were filled by reflecting the image outward toward the edges and corners.

Encoder (MNIST 48×48)			
Layer	Channels	Kernel	Stride
Convolution	32	3×3	1
Conv block	64	3×3	2
Conv block	128	3×3	2
Conv block	256	3×3	2
Conv block	512	3×3	2
Norm+ReLU			

Table 2: The encoder used for all models with MNIST 48×48 .

Decoder (MNIST 48×48)			
Layer	Channels	Kernel	Stride
Convolution	256	3×3	1
Conv block	128	3×3	1
Conv block	64	3×3	1
Conv block	32	3×3	1
Norm+ReLU+Conv	1	3×3	1

Table 3: The decoder used for all models (*common* but not *residual* decoder in the proposed method) with MNIST 48×48 .

Residual decoder (MNIST 48×48)			
Layer	Channels	Kernel	Stride
Convolution	256	5×5	1
Conv block (no short skip)	128	5×5	1
Conv block (no short skip)	64	5×5	1
Conv block (no short skip)	32	5×5	1
Norm+ReLU+Conv	1	5×5	1

Table 4: The *residual* decoder used in the proposed method with MNIST 48×48 .

Encoder (MNIST 128×128 and BraTS)

Layer	Channels	Kernel	Stride
Convolution	16	3×3	1
Conv block	32	3×3	2
Conv block	64	3×3	2
Conv block	128	3×3	2
Conv block	256	3×3	2
Conv block	512	3×3	2
Norm+ReLU			

Table 5: The encoder used for all models with MNIST 128×128 and BraTS.

Decoder (MNIST 128×128 and BraTS)

Layer	Channels	Kernel	Stride
Convolution	256	3×3	1
Conv block	128	3×3	1
Conv block	64	3×3	1
Conv block	32	3×3	1
Conv block	16	3×3	1
Norm+ReLU+Conv	1	3×3	1

Table 6: The decoder used for all models (*common* but not *residual* decoder in the proposed method) with MNIST 128×128 and BraTS.**Residual decoder (MNIST 128×128 and BraTS)**

Layer	Channels	Kernel	Stride
Convolution	256	5×5	1
Conv block (no short skip)	128	5×5	1
Conv block (no short skip)	64	5×5	1
Conv block (no short skip)	32	5×5	1
Conv block (no short skip)	16	5×5	1
Norm+ReLU+Conv	1	5×5	1

Table 7: The *residual* decoder used in the proposed method with MNIST 128×128 and BraTS.**Discriminator (MNIST)**

Layer	Channels	Kernel	Stride
Convolution	128	4×4	1
Norm+ReLU+Conv	128	4×4	2
Norm+ReLU+Conv	256	4×4	2
Norm+ReLU+Conv	512	4×4	2
Convolution	1	1×1	1

Table 8: The discriminator used in the proposed method with MNIST 48×48 and 128×128.

Discriminator (BraTS)

Layer	Channels	Kernel	Stride
Convolution	64	4×4	1
Norm+ReLU+Conv	64	4×4	2
Norm+ReLU+Conv	128	4×4	2
Norm+ReLU+Conv	256	4×4	2
Norm+ReLU+Conv	512	4×4	2
Convolution	1	1×1	1

Table 9: The discriminator used in the proposed method with BraTS.